# Stability Analysis of a Three-Input Three-Output Multi-Converters for Energy Management System

Toshiyuki Fujita
*Graduate School of Frontier Sciences*
*the University of Tokyo*
Chiba, Japan
t-fujita@edu.k.u-tokyo.ac.jp

Masahiro Mae
*Electrical Engineering and Information Systems*
*the University of Tokyo*
Tokyo, Japan

Hiroshi Fujimoto
*Graduate School of Frontier Sciences*
*the University of Tokyo*
Chiba, Japan

Michihiro Nakagawa, Yashiki Yasuda, Akio Yamagiwa
*Technology and Innovation Center*
*DAIKIN INDUSTRIES, LTD.*
Osaka, Japan

***Abstract*—Dc-dc converters are essential components in various energy conversion applications. Connecting multiple converters to a common dc link is a common configuration in various applications, including dc microgrids, ships, electric vehicles, data centers, and home energy management systems. This paper analyzes boost and buck dc-dc converters connected to a shared dc link capacitor with a multi-input multi-output (MIMO) architecture for a home energy management system. State space equations were constructed using a state space averaging method. The transfer function was calculated from these equations, demonstrating the interference between each converter. The experimental setup was constructed and verified to the analytical model. The frequency response data was obtained by a system identification experimentally. Experimental validation confirms the model's accuracy in representing the system's dynamics. However, MIMO Nyquist stability analysis with generalized Gershgorin bands reveals potential instability with conventional control methods due to MIMO interactions. Performing the step response of the system also reveals interaction between each converter.**

***Index Terms*—current control, MIMO converter, MIMO stability analysis, Nyquist analysis.**

## I. Introduction

Dc-dc converters are widely installed in various applications. Their increasing efficiency, integration, and miniaturization, coupled with the benefits of connecting multiple converters to a common dc link capacitor, have made this configuration prevalent in applications such as ships, EVs, data centers, and home energy management systems (HEMS) [1]. These energy management systems (EMS), including HEMS [2], building EMS, factory EMS, and vehicle-to-home systems, manage power flow between renewable energy sources, battery storage, and the grid. A multi-input multi-output (MIMO) converter is controlled by using sliding mode control for each current [3]. However, these systems are inherently MIMO converters, and current control design often simplifies the problem by treating inter-converter interactions as disturbances or feedforward signals, rather than addressing the full MIMO nature of the system.

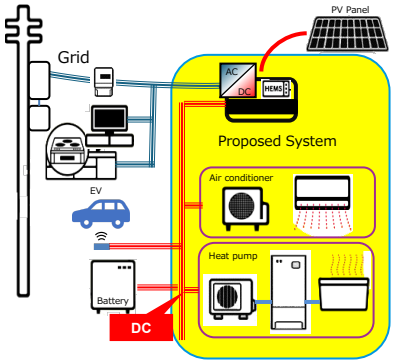


Fig. 1: Concept of the proposed system.

Droop control, widely used in grid-connected systems, is known for its robustness and stability; one study, for instance, analyzed its stability for AC grid-connected inverters [4]. However, it's not ideal for precise current control because command value errors persist even after system convergence.

The presence of Constant Power Loads (CPLs)—e.g., motor drives—on a DC bus often leads to stability challenges. A CPL's negative incremental impedance means its input current decreases as input voltage increases [5]. This can induce limit cycles, resulting in higher current and voltage ripples that degrade semiconductor devices. Numerous solutions have been proposed for this voltage instability, including impedance specification methods [6], Nonlinear PWM Control [7], and passivity-based control (e.g., with extended Kalman filters [8] or nonlinear observers [9]). However, comprehensive experimental approaches to address this instability have not been fully established, and existing methods only focus on single-converter performance.

Fig. 1 shows our concept of the Energy Management System (EMS). An EMS was developed that brings together high-power household electrical equipment (over 1 kW)—including

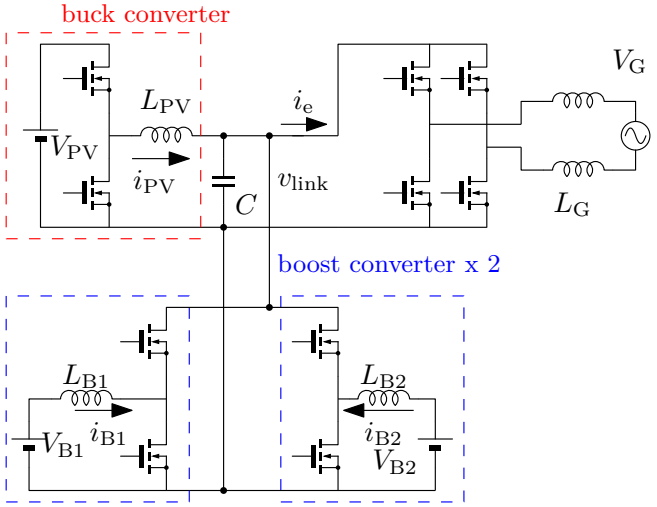


Fig. 2: Analyzed system of this paper. which is connected in the same dc link capacitor. One buck converter, two boost converters, and a grid-connected inverter.

PV panels, battery systems, air conditioners, grid-connected inverters, and EV chargers—into a single, unified control box. The goal of this paper is to verify the EMS's stability and enhance its responsiveness. As a standard practice, PV converters are typically buck converters, and battery converters are boost converters.

This paper studies MIMO theory for MIMO converter employing boost and buck dc-dc converters connected to a shared dc link capacitor. State space equations were constructed using a state space averaging method. The transfer function was calculated from these equations demonstrating the interference between each converter. The experimental setup was constructed and verified using the analytical model. The frequency response data was estimated to compare the calculated transfer function by the system identification experimentally. Experimental validation confirms the model's accuracy in representing the system's dynamics. MIMO stability was analyzed using Nyquist plots that incorporated generalized Gershgorin bands. This stability was verified further with Single-Input Single-Output (SISO) Nyquist plots, again leveraging the generalized Gershgorin bands. The evaluation of a step response also confirmed the behavior of the interferences, showing that other inputs influenced the current.

## II. Modeling and Analysis of the MIMO Converter

Fig. 2 shows the analyzed system of this paper. which is connected to the same dc link capacitor. One buck converter, two boost converters, and a grid-connected inverter. The parameters of the system are defined in Fig. 2 , respectively. Parasitic resistances of the reactors are $r_i$, where $i$ denominates the individual converter.

Kirchhoff's laws yield the following equation, which is applied to the system depicted in Fig. 2:

$$\frac{\mathrm{d}}{\mathrm{d}t}x = f(x,u) = \begin{pmatrix} \frac{d_{\mathrm{PV}}}{L_{\mathrm{PV}}}V_{\mathrm{PV}} - \frac{r_{\mathrm{PV}}}{L_{\mathrm{PV}}} - \frac{v_{\mathrm{link}}}{L_{\mathrm{PV}}} \\ -\frac{r_{\mathrm{B1}}}{L_{\mathrm{B1}}}i_{\mathrm{B1}} - \frac{d_{\mathrm{B1}}}{L_{\mathrm{B1}}}v_{\mathrm{link}} + \frac{V_{\mathrm{B1}}}{L_{\mathrm{B1}}} \\ -\frac{r_{\mathrm{B2}}}{L_{\mathrm{B2}}}i_{\mathrm{B2}} - \frac{d_{\mathrm{B2}}}{L_{\mathrm{B2}}}v_{\mathrm{link}} + \frac{Vt_{\mathrm{B2}}}{L_{\mathrm{B2}}} \\ \frac{i_{\mathrm{PV}}}{C} + \frac{d_{\mathrm{B1}}}{C}i_{\mathrm{B1}} + \frac{d_{\mathrm{B2}}}{C}i_{\mathrm{B2}} - \frac{i_e}{C} \end{pmatrix}. \quad (1)$$

where

$$\begin{aligned} x &= \begin{pmatrix} i_{\mathrm{PV}} & i_{\mathrm{B1}} & i_{\mathrm{B2}} & v_{\mathrm{link}} \end{pmatrix}^{\mathrm{T}}, \\ u &= \begin{pmatrix} d_{\mathrm{PV}} & d_{\mathrm{B1}} & d_{\mathrm{B2}} \end{pmatrix}^{\mathrm{T}}. \end{aligned}$$

Linearized Eq. (1) around the steady-state operating point yields the following small-signal state-space representation: (2) and (3).

$$\begin{aligned} \frac{d}{dt}\Delta x &= \Delta A \Delta x + \Delta B \Delta d, & (2) \\ \Delta y &= \Delta C \Delta x, & (3) \end{aligned}$$

where

$$\begin{aligned} \Delta x &= \Delta y = \begin{pmatrix} \Delta i_{\mathrm{PV}} & \Delta i_{\mathrm{B1}} & \Delta i_{\mathrm{B2}} & \Delta v_{\mathrm{link}} \end{pmatrix}^{\mathrm{T}}, \\ \Delta d &= \begin{pmatrix} \Delta d_{\mathrm{PV}} & \Delta d_{\mathrm{B1}} & \Delta d_{\mathrm{B2}} \end{pmatrix}^{\mathrm{T}}, \\ \Delta A &= \frac{\partial f}{\partial x} \\ &= \begin{pmatrix} -\frac{r_{\mathrm{PV}}}{L_{\mathrm{PV}}} & 0 & 0 & -\frac{1}{L_{\mathrm{PV}}} \\ 0 & -\frac{r_{\mathrm{B1}}}{L_{\mathrm{B1}}} & 0 & -\frac{D_{\mathrm{B1}}}{L_{\mathrm{B1}}} \\ 0 & 0 & -\frac{r_{\mathrm{B2}}}{L_{\mathrm{B2}}} & -\frac{D_{\mathrm{B2}}}{L_{\mathrm{B2}}} \\ \frac{1}{C} & \frac{D_{\mathrm{B1}}}{C} & \frac{D_{\mathrm{B2}}}{C} & 0 \end{pmatrix}, \\ \Delta B &= \frac{\partial f}{\partial d} \\ &= \begin{pmatrix} \frac{V_{\mathrm{PV}}}{L_{\mathrm{PV}}} & 0 & 0 \\ 0 & -\frac{V_{\mathrm{link}}}{L_{\mathrm{B1}}} & 0 \\ 0 & 0 & -\frac{V_{\mathrm{link}}}{L_{\mathrm{B2}}} \\ 0 & \frac{I_{\mathrm{B1}}}{C} & \frac{I_{\mathrm{B2}}}{C} \end{pmatrix}, \\ \Delta C &= I. \end{aligned}$$

The transfer functions of Eqs. (2), (3), relating the inputs $\Delta d$ to the outputs $\Delta y$ are given by:

$$\begin{aligned} G &= \frac{\Delta y}{\Delta d} = \Delta C(sI - \Delta A)^{-1}\Delta B. & (4) \\ &= \begin{pmatrix} G_{11} & G_{21} & G_{31} \\ G_{12} & G_{22} & G_{32} \\ G_{13} & G_{23} & G_{33} \\ G_{14} & G_{24} & G_{34} \end{pmatrix} \end{aligned}$$

The elements of the transfer function $G_{ij}$ are as follows:

$$\begin{aligned} G_{11} &= \Big\{ L_{\mathrm{PV}}(L_{\mathrm{B1}}s + r_{\mathrm{B1}})(L_{\mathrm{B2}}s + r_{\mathrm{B2}})Cs \\ &\quad + L_{\mathrm{PV}}D_{\mathrm{B2}}^2(L_{\mathrm{B1}}s + r_{\mathrm{B1}}) + D_{\mathrm{B1}}^2(L_{\mathrm{B2}}s + r_{\mathrm{B2}})V_{\mathrm{PV}} \Big\}\Psi^{-1} \\ G_{21} &= (L_{\mathrm{B2}}s + r_{\mathrm{B2}})\frac{D_{\mathrm{B1}}V_{\mathrm{link}} - (L_{\mathrm{B1}}s + r_{\mathrm{B1}})I_{\mathrm{B1}}}{\Psi} \end{aligned}$$

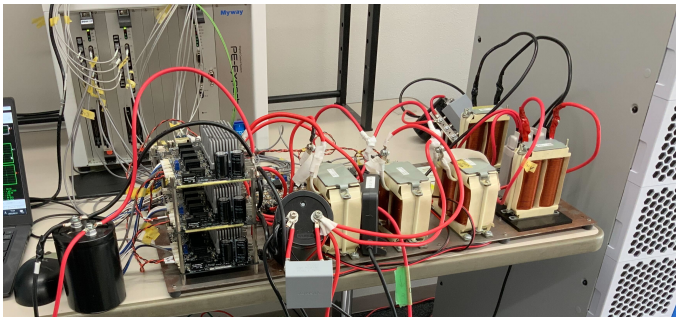

Fig. 3: Photograph of experimental system shown in Fig. 2.

$$
\begin{aligned}
G_{31} &= (L_{\mathrm{B1}}s + r_{\mathrm{B1}})\frac{D_{\mathrm{B2}}V_{\mathrm{link}} - (L_{\mathrm{B2}}s + r_{\mathrm{B2}})I_{\mathrm{B2}}}{\Psi} \\
G_{12} &= -\frac{D_{\mathrm{B1}}(L_{\mathrm{B2}}s + r_{\mathrm{B2}})V_{\mathrm{PV}}}{\Psi} \\
G_{22} &= -\Big\{(CV_{\mathrm{link}}s + D_{\mathrm{B1}}I_{\mathrm{B1}})(L_{\mathrm{PV}}s + r_{\mathrm{PV}})(L_{\mathrm{B2}}s + r_{\mathrm{B2}}) \\
&\quad + D_{\mathrm{B2}}^2(L_{\mathrm{PV}}s + r_{\mathrm{PV}})V_{\mathrm{link}} + (L_{\mathrm{B2}}s + r_{\mathrm{B2}})V_{\mathrm{link}}\Big\}\Psi^{-1} \\
G_{32} &= \Big\{D_{\mathrm{B1}}D_{\mathrm{B2}}(L_{\mathrm{PV}}s + r_{\mathrm{PV}})V_{\mathrm{link}} \\
&\quad - D_{\mathrm{B1}}(L_{\mathrm{PV}}s + r_{\mathrm{PV}})(L_{\mathrm{B2}}s + r_{\mathrm{B2}})I_{\mathrm{B2}}\Big\}\Psi^{-1} \\
G_{13} &= -\frac{D_{\mathrm{B2}}(L_{\mathrm{B1}}s + r_{\mathrm{B1}})V_{\mathrm{PV}}}{\Psi} \\
G_{23} &= \Big\{D_{\mathrm{B1}}D_{\mathrm{B2}}(L_{\mathrm{PV}}s + r_{\mathrm{PV}})V_{\mathrm{link}} \\
&\quad - D_{\mathrm{B2}}(L_{\mathrm{PV}}s + r_{\mathrm{PV}})(L_{\mathrm{B1}}s + r_{\mathrm{B1}})I_{\mathrm{B1}}\Big\}\Psi^{-1} \\
G_{33} &= -\Big\{(CV_{\mathrm{link}}s + D_{\mathrm{B2}}I_{\mathrm{B2}})(L_{\mathrm{PV}}s + r_{\mathrm{PV}})(L_{\mathrm{B1}}s + r_{\mathrm{B1}}) \\
&\quad + D_{\mathrm{B1}}^2(L_{\mathrm{PV}}s + r_{\mathrm{PV}})V_{\mathrm{link}} + (L_{\mathrm{B1}}s + r_{\mathrm{B1}})V_{\mathrm{link}}\Big\}\Psi^{-1} \\
G_{14} &= \frac{(L_{\mathrm{B1}}s + r_{\mathrm{B1}})(L_{\mathrm{B2}}s + r_{\mathrm{B2}})V_{\mathrm{PV}}}{\Psi} \\
&\quad \Big\{(L_{\mathrm{B2}}s + r_{\mathrm{B2}})I_{\mathrm{B2}} - D_{\mathrm{B2}}V_{\mathrm{link}}\Big\} \\
G_{24} &= \frac{(L_{\mathrm{PV}}s + r_{\mathrm{PV}})(L_{\mathrm{B2}}s + r_{\mathrm{B2}})}{\Psi}\times \\
&\quad \Big\{(L_{\mathrm{B1}}s + r_{\mathrm{B1}})I_{\mathrm{B1}} - D_{\mathrm{B1}}V_{\mathrm{link}}\Big\} \\
G_{34} &= \frac{(L_{\mathrm{PV}}s + r_{\mathrm{PV}})(L_{\mathrm{B1}}s + r_{\mathrm{B1}})}{\Psi}\times \\
&\quad \Big\{(L_{\mathrm{B2}}s + r_{\mathrm{B2}})I_{\mathrm{B2}} - D_{\mathrm{B2}}V_{\mathrm{link}}\Big\}
\end{aligned}
$$

where

$$
\begin{aligned}
\Psi = (L_{\mathrm{PV}}s + r_{\mathrm{PV}})\Big\{&Cs(L_{\mathrm{B1}}s + r_{\mathrm{B1}})(L_{\mathrm{B2}}s + r_{\mathrm{B2}}) \\
&+ D_{\mathrm{B1}}^2(L_{\mathrm{B2}}s + r_{\mathrm{B2}}) + D_{\mathrm{B2}}^2(L_{\mathrm{B1}}s + r_{\mathrm{B1}})\Big\} \\
&+ (L_{\mathrm{B1}}s + r_{\mathrm{B1}})(L_{\mathrm{B2}}s + r_{\mathrm{B2}})
\end{aligned}
$$

The off-diagonal terms are not equal to zero, these terms cause the interference between each converter. In other words, the transfer function $G$ represents the dynamics of the MIMO converter and does not consider the controllability of the system.

TABLE I: Parameters of the system.

| Parameter | Value | Parameter | Value |
|---|---|---|---|
| $L_{\mathrm{H}}$ | 1.23 mH | $r_{\mathrm{H}}$ | 0.328 Ω |
| $L_{\mathrm{L}}$ | 438 $\mu$H | $r_{\mathrm{L}}$ | 0.206 Ω |
| $L_{\mathrm{L}}$ | 438 $\mu$H | $r_{\mathrm{L}}$ | 0.206 Ω |
| $L_{\mathrm{G}}$ | 438 $\mu$H | $r_{\mathrm{G}}$ | 0.206 Ω |
| $C_{\mathrm{link}}$ | 712 nF | $f_{\mathrm{sw}}$ | 20 kHz |
| $V_{\mathrm{H}}$ | 200 V | $V_{\mathrm{L}}$ | 100 V |
| $V_{\mathrm{L}}$ | 100 V | $V_{\mathrm{G}}$ | 200 Vrms |

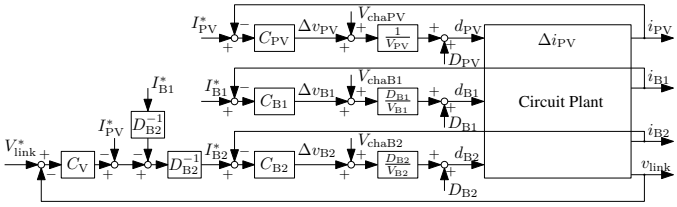


Fig. 4: Block diagram of the whole system in the system identification.

## III. Experimental Result

Fig. 3 shows the experimental system shown in Fig. 2. Table I lists the system's circuit parameters, measured at 20 kHz. A Myway Plus PE-Expert4 (MWPE4-PEV) controller is used for all experiments, with a calculation period equal to the carrier frequency $f_{\mathrm{sw}}$. Large electrolytic capacitors are placed on $V_{\mathrm{PV}}$ and $V_{\mathrm{B}}$ to stabilize the system identification.

### A. System Identification

Fig. 4 shows the block diagram of the system in the system identification. The identification was confirmed using one chirp signal $V_{\mathrm{chax}}$ in each input with the conditions of the disturbance current $i_e$=0, and the other chirp signals are zero. In other words, three experiments are required to perform 3x3 system identification. The controllers of the converters are designed below:

$$
C_x = K_{\mathrm{P}x} + \frac{K_{\mathrm{I}x}}{s} \tag{5}
$$

The PI gains of the converters $C_x$ shown in Fig. 4 are designed using the pole placement method of the single converters, and the parameters are below:

$$
\begin{aligned}
K_{\mathrm{PPV}} &= \omega_{\mathrm{C}}L_{\mathrm{PV}} - r_{\mathrm{PV}}, \quad K_{\mathrm{IPV}} = \omega_{\mathrm{C}}^2 L_{\mathrm{PV}}, && (6)\\
K_{\mathrm{PB1}} &= \omega_{\mathrm{C}}L_{\mathrm{B1}} - r_{\mathrm{B1}}, \quad K_{\mathrm{IB1}} = \omega_{\mathrm{C}}^2 L_{\mathrm{PV}}, && (7)\\
K_{\mathrm{PB2}} &= \omega_{\mathrm{C}}L_{\mathrm{B2}} - r_{\mathrm{B2}}, \quad K_{\mathrm{IB2}} = \omega_{\mathrm{C}}^2 L_{\mathrm{B2}}, && (8)\\
K_{\mathrm{PV}} &= \omega_{\mathrm{V}}C_{\mathrm{link}}, \quad K_{\mathrm{IB2}} = \omega_{\mathrm{V}}^2 C_{\mathrm{link}}. && (9)
\end{aligned}
$$

Where $\omega_{\mathrm{C}}$ and $\omega_{\mathrm{V}}$ are the angular cutoff frequency, which is the same meaning as the pole of the feedback control system. To identify the accurate system, feedback control is installed which maintains the operating point. $\omega_{\mathrm{C}}$ and $\omega_{\mathrm{V}}$ need to be small compared to the frequency at which the system identification is performed. In this system identification, $\omega_{\mathrm{C}}$ are $2\pi \times 21$ rad/s and $\omega_{\mathrm{V}}$ is $2\pi \times 7$ rad/s.

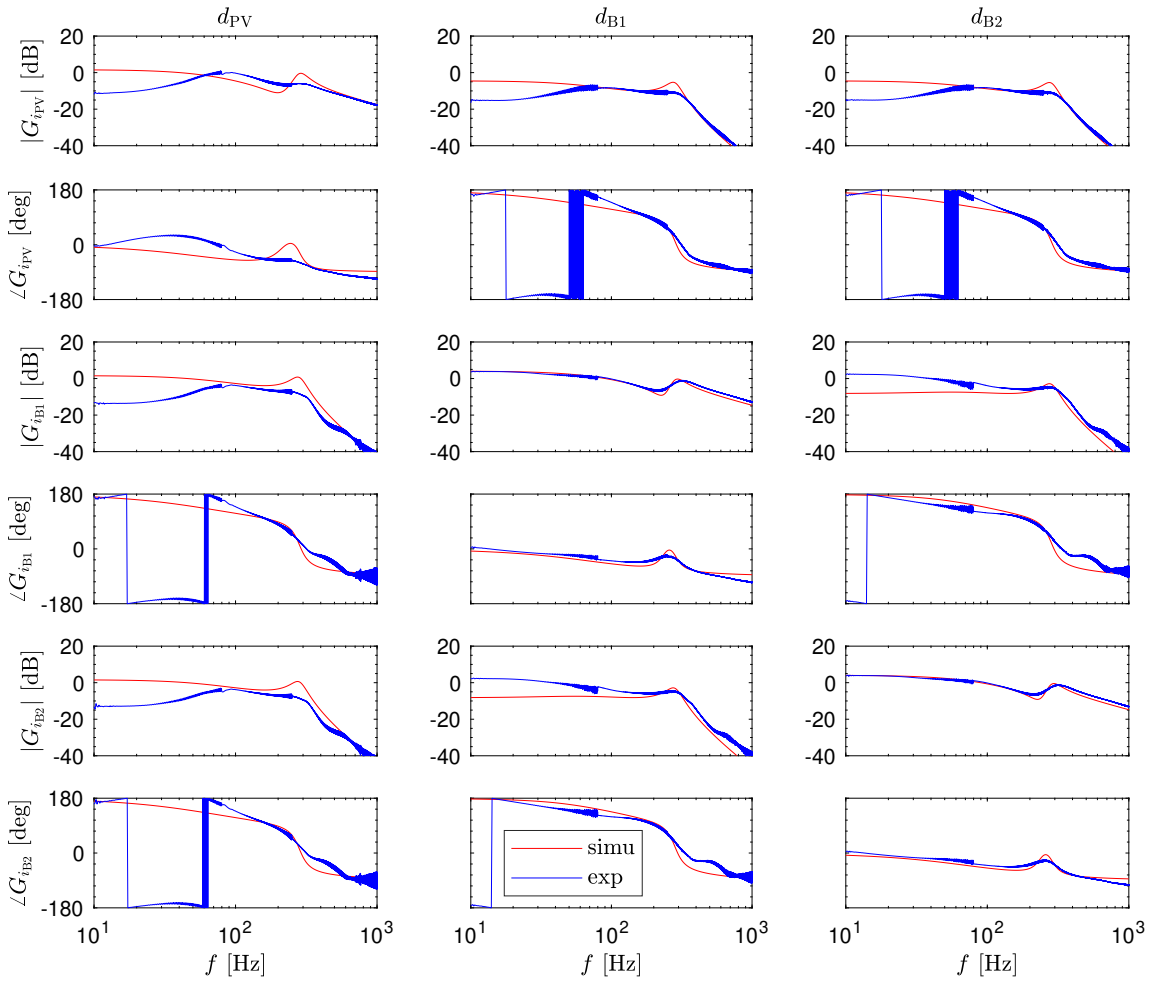


Fig. 5: Bode plots of the system with experimental system identification of the system, and calculation of transfer functions used in Eq. (4) of $G_{11}$ to $G_{33}$.

### *B. Bode Plots*

Fig. 5 is the Bode plots of the system with experimental system identification and calculation result used in Eq. (4). The simulation and the experimental result generally agree well, especially in the high frequency range. Also, the frequencies of resonance and anti-resonance points coincide between the experiments and calculations. The off-diagonal terms of the experimental results are also not equal to zero, in other words, these terms cause the interference between each converter. The difference between the experimental result and model-based calculation in Eq (4) is due to the influence of parameters such as the dead time of the switching device, the internal impedance of the constant voltage source, and the feedback effect of the cutoff frequency discussed above, which are not taken into account in the calculation.

### *C. Nyquist Plots*

Nyquist plot is widely used to analyze the stability of a feedback control system and is created by plotting the vector locus of the open-loop transfer function $GC$, which is derived from the transfer functions of the system $G$ in Fig. 5 and the controller $C$ in Eq. (5). The current controllers of the converters for drawing the Nyquist plots are used in the PI control, where $\omega_{\mathrm{C}}$ is $2\pi \times 200$ rad/s. Generalized Gershgorin bands are a sufficient condition for the range within which the Nyquist plot may shift at the angular frequency point due to the influence of other axes [10]. In other words, the Nyquist plot can move within a circular range due to the interference of the other converter.

Fig. 6 shows the SISO Nyquist plots with generalized Gershgorin bands of the transfer function shown in Eq. (4) and current controller $C$. The SISO Nyquist plots are stable shown in Fig. 7. However, the generalized Gershgorin bands contain $(-1, \mathrm{j}0)$ in each axis. This means the overall control system might be unstable.

Fig. 7 shows the SISO Nyquist plots with generalized Gershgorin bands for the experimental frequency response data presented in Fig. 5 and the current controller $C$. The overall trend aligns with the simulation data, and the discussions remain consistent with those from the simulation. However,

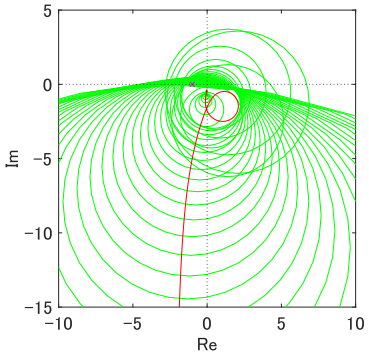


(a)

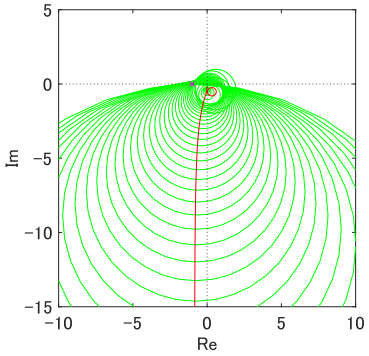


(b)

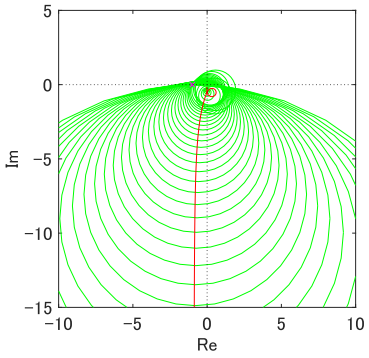


(c)

Fig. 6: Simulation results of Nyquist plots with generalized Gershgorin bands of which transfer function is shown in Eq. (4) and PI current control. And the magenta x is the (0, -$j$) point. (a) from $d_{\mathrm{PV}}$ to $i_{\mathrm{PV}}$. (b) from $V_{\mathrm{B1}}$ to $i_{\mathrm{B1}}$.(b) from $V_{\mathrm{B2}}$ to $i_{\mathrm{B2}}$.

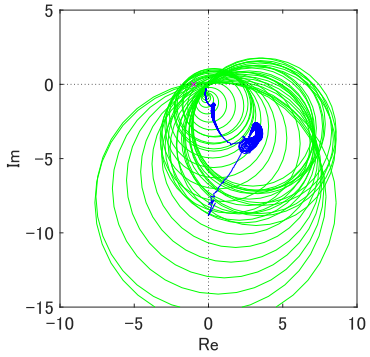


(a)

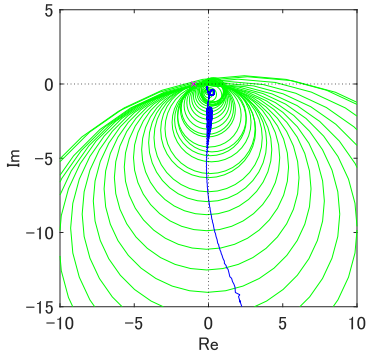


(b)

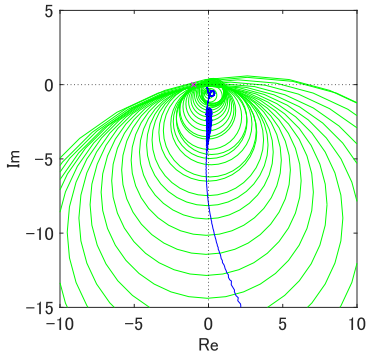


(c)

Fig. 7: Nyquist plots with generalized Gershgorin bands of experimental frequency response data in Fig. 5 and simulated PI current control. And the magenda x is the (0, -$j$) point. (a) from $d_{\mathrm{PV}}$ to $i_{\mathrm{PV}}$. (b) from $V_{\mathrm{B1}}$ to $i_{\mathrm{B1}}$.(b) from $V_{\mathrm{B2}}$ to $i_{\mathrm{B2}}$.

differences are observable in the Nyquist plot, particularly in the low-frequency response data on the PV side.

### *D. Step Response of the System*

Fig. 8 shows the current step response of $i_{\mathrm{PV}}$ from 6 A to 3 A for the system depicted in Fig. 2 and 4. The current controller, defined by Eq. (6)-(8), uses an angular frequency $\omega_{\mathrm{C}}$ of $2\pi \times 200$ rad/s. The voltage controller, given by Eq. (9), has an $\omega_{\mathrm{V}}$ of $2\pi \times 20$ rad/s. Following the step response, fluctuations occurred in all voltages and currents, including $i_{\mathrm{PV}}$. This is because the step change in the PV current $i_{\mathrm{PV}}$ alters the DC link voltage $v_{\mathrm{link}}$, which subsequently impacts the current of the other converters. These observed fluctuations are a result of this mutual interference.

## IV. Conclusion and Future Work

This paper analyzes the MIMO converter using MIMO theory and Nyquist plots with generalized Gershgorin bands. The system analyzed a small signal state space equation from the circuit equations. The calculated transfer function from the state-space equations has mutual interference for

each axis. System identification has been performed to derive frequency response data and compare the calculated transfer function. The theory and experimental results of the transfer function and frequency response data were consistent, and the system still had interference between each input. The SISO Nyquist plots revealed that the system was stable. However, considering generalized Gershgorin bands, the system might be unstable for the influence of other inputs. The step response data has been verified and the interference of the system was observed as the fluctuations of the measured values.

## REFERENCES


[1] H. Watanabe, K. Yamanokuchi, Y. Ikeda, Y. Takahashi, and J.-i. Itoh, "Universal smart power module (uspm) for carbon neutral society," *IEEE Transactions on Industry Applications*, vol. 60, no. 2, pp. 3411–3417, 2024.

[2] A. Sangswang and M. Konghirun, "Optimal strategies in home energy management system integrating solar power, energy storage, and vehicle-to-grid for grid support and energy efficiency," *IEEE Transactions on Industry Applications*, vol. 56, no. 5, pp. 5716–5728, 2020.

[3] G. Garraffa, A. Accetta, M. Luna, M. Pucci, F. Alonge, and A. Sferlazza, "Indirect sliding mode control of a mimo modular converter for dc microgrids: a rov case study," in *2024 IEEE Energy Conversion Congress and Exposition (ECCE)*, 2024, pp. 3659–3664.

[4] Y. Mitsugi and J. Baba, "Phaser-based transfer function analysis of power synchronization control instability for a grid forming inverter in a stiff grid," *IEEE Access*, vol. 11, pp. 42 146–42 159, 2023.

[5] A. Emadi, A. Khaligh, C. Rivetta, and G. Williamson, "Constant power loads and negative impedance instability in automotive systems: definition, modeling, stability, and control of power electronic converters and motor drives," *IEEE Transactions on Vehicular Technology*, vol. 55, no. 4, pp. 1112–1125, 2006.

[6] B. He, W. Chen, C. Zhang, Y. Yuan, and C. Zhang, "Impedance specifications for stability design of grid-connected dc distribution power systems," *IEEE Transactions on Industrial Electronics*, vol. 71, no. 6, pp. 5830–5843, 2024.

[7] B. A. Martínez-Treviño, A. E. Aroudi, H. Valderrama-Blavi, A. Cid-Pastor, E. Vidal-Idiarte, and L. Martinez-Salamero, "PWM nonlinear control with load power estimation for output voltage regulation of a boost converter with constant power load," *IEEE Transactions on Power Electronics*, vol. 36, no. 2, pp. 2143–2153, 2021.

[8] M. Abdolahi, J. Adabi, and S. Y. M. Mousavi, "An adaptive extended kalman filter with passivity-based control for dc-dc converter in dc microgrids supplying constant power loads," *IEEE Transactions on Industrial Electronics*, vol. 71, no. 5, pp. 4873–4882, 2024.

[9] M. A. Hassan, C.-L. Su, F.-Z. Chen, and K.-Y. Lo, "Adaptive passivity-based control of a dc–dc boost power converter supplying constant power and constant voltage loads," *IEEE Transactions on Industrial Electronics*, vol. 69, no. 6, pp. 6204–6214, 2022.

[10] S. Skogestad and I. Postlethwaite, *Multivariable Feedback Control*, 2nd ed. John Wiley and Sons Ltd., 2005.


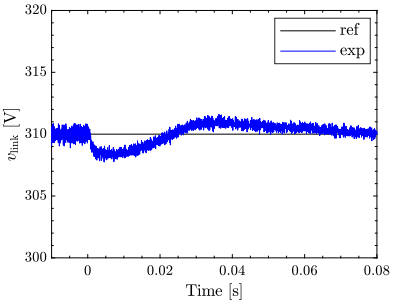


(a)

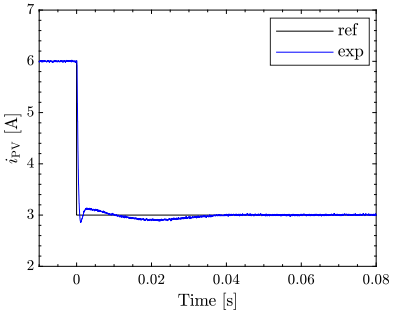


(b)

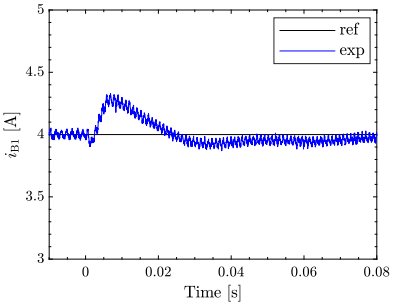


(c)

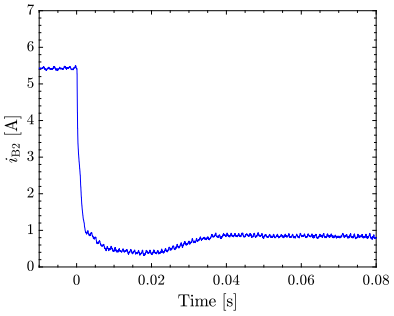


(d)

Fig. 8: Nyquist plots with generalized Gershgorin bands of experimental transfer function data and simulated PI current control. And the magenda x is the (0, -$j$) point. (a) from $d_{\text{PV}}$ to $i_{\text{PV}}$. (b) from $V_{\text{B1}}$ to $i_{\text{B1}}$.(b) from $V_{\text{B2}}$ to $i_{\text{B2}}$.